Transparent Gradient-Index Lens for Underwater Sound Based on Phase Advance

Theodore P. Martin,* Christina J. Naify, Elizabeth A. Skerritt, Christopher N. Layman, Michael Nicholas, David C. Calvo, and Gregory J. Orris

U.S. Naval Research Laboratory, Code 7160, Washington, D.C. 20375, USA

Daniel Torrent and José Sánchez-Dehesa

Department of Electronic Engineering, Wave Phenomena Group, Universidad Politecnica de Valencia, C/ Camino de Vera s7n, E-46002 Valencia, Spain

(Received 23 April 2015; revised manuscript received 20 May 2015; published 15 September 2015)

Spatial gradients in a refractive index are used extensively in acoustic metamaterial applications to control wave propagation through phase delay. This study reports the design and experimental realization of an acoustic gradient-index lens using a sonic crystal lattice that is impedance matched to water over a broad bandwidth. In contrast to previous designs, the underlying lattice features refractive indices that are lower than the water background, which facilitates propagation control based on a phase advance as opposed to a delay. The index gradient is achieved by varying the filling fraction of hollow, air-filled aluminum tubes that individually exhibit a higher sound speed than water and matched impedance. Acoustic focusing is observed over a broad bandwidth of frequencies in the homogenization limit of the lattice, with intensity magnifications in excess of 7 dB. An anisotropic lattice design facilitates a flat-faceted geometry with low backscattering at 18 dB below the incident sound-pressure level. A three-dimensional Rayleigh-Sommerfeld integration that accounts for the anisotropic refraction is used to accurately predict the experimentally measured focal patterns.

DOI: 10.1103/PhysRevApplied.4.034003

I. INTRODUCTION

Metamaterial lattices composed of subwavelength scattering components have been used increasingly in recent years to control the propagation of both electromagnetic and acoustic waves through two and three dimensions. One primary goal of acoustic metamaterial design is to achieve effective fluid, or "metafluid," material properties that minimize shear coupling and propagation. The coupling between a fluid-borne acoustic wave and a composite elastic material at off-normal incidence results in mode mixing of dilatation and shear modes that complicates the interaction. For underwater applications requiring strong acoustic coupling, compliant materials such as rubbers are a standard material used for coupling and encapsulation due to their relatively close impedance match with water and low shear moduli. Traditional compliant materials often have larger densities and/or lower dilatation moduli than water, making them useful for applications requiring a low relative sound speed. For example, a sonic crystal lattice of rubber cylinders with a gradient filling fraction was recently used to achieve an underwater omnidirectional absorption coating [1], which requires a radially decreasing sound speed [2,3].

Metafluids with complementary material properties compared to rubbers, e.g., high relative sound speeds with matched impedance, are more difficult to achieve in underwater applications, because they require high stiffness but low relative density. Sonic crystal lattices feature metafluid functionality in the homogenization limit of the lattice, including shear decoupling and broadband performance, and hence they have the potential to expand the range of realizable metafluid material properties to include high sound speeds. Thin-walled, hollow elastic shells have been recently proposed as high-sound-speed sonic crystal components in water [4]. By carefully tuning the wall thickness of the shell, an impedance-matched condition can be obtained, assuming the shell material has a higher impedance than the background fluid. Additionally, by using shell elements which are individually impedance matched, it has been shown that any phononic crystal configuration of the elements will also be impedance matched in the homogenization limit of the crystal lattice [4]. Given that local variations in the element filling fraction create a variation in the refractive index, acoustically transparent devices with tunable wave-guiding capability should be achievable using hollow-shell elements. The concept of hollow-shell elements is also extended to include structural components inside the shells to improve control over the material properties [5].

Here we report the design and experimental demonstration of an acoustically transparent gradient-index (GRIN) lens that focuses sound by *advancing* the phase of waves propagating through an aqueous background. GRIN geometries are utilized for a broad range of metamaterial applications including scattering reduction [6,7], wave focusing [8–16], and bending [1–3,17,18]. In contrast to

*theodore.martin@nrl.navy.mil

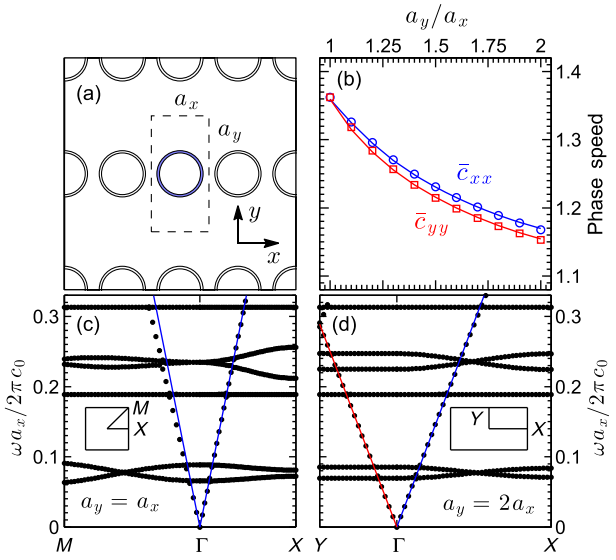

FIG. 1. (a) Schematic unit cell of the anisotropic lattice with $a_y = 2a_x$. (b) Phase speeds in the homogenization limit of the lattice plotted as a function of anisotropy ratio a_y/a_x. Lines are fits to the data based on Ref. [21]. (c) Acoustic band structure calculated using the finite-element method for an isotropic lattice with tube outer radius $R = 0.4a_x$. Blue lines plot the acoustic sound speed in the ΓX direction. (d) Acoustic band structure calculated for an anisotropic lattice with tube outer radius $R = 0.4a_x$. Blue and red lines plot the acoustic sound speed in the ΓX and ΓY directions, respectively. Insets show the directions of the bands in k space.

previous lens designs, we present a lens composed of impedance-matched, hollow-shell elements with sound speeds higher than water. The higher sound speed enables the phase of propagating waves to be advanced beyond what is possible in the background propagation medium, which is important to a number of metamaterial applications (for a review, see Refs. [19,20]). The lens is intended as a proof of concept to demonstrate that both transparency and broadband wave-guiding functionality can be achieved simultaneously using a lattice of noncompliant, low-refractive-index scattering elements.

II. LENS DESIGN

The GRIN lens is constructed using cylindrical, air-filled aluminum tubes arranged in a lattice that function as a broadband, uniform effective medium at wavelengths λ larger than the lattice spacing a ($\lambda > 4a$). With a wall thickness of 1/20th the diameter, each individual cylindrical tube scatters sound as an impedance-matched effective fluid cylinder [4], resulting in negligible backscattering over the lattice as a whole. An anisotropic lattice spacing is used to vary the filling fraction similar to what was proposed by Lin, Tittmann, and Huang [14]. The anisotropic design simplifies the lens construction by using a single cylindrical tube geometry and features a flat lens facet. While the objective of many metafluid applications is to achieve anisotropy in the wave speed, the transparency of the lattice results in an approximately isotropic scattering configuration despite the underlying anisotropy of the design. Our design goal is to tune the anisotropy to produce a convex refraction gradient that focuses sound while simultaneously minimizing lens aberration.

Figure 1(a) shows the rectangular unit cell of the cylinder lattice. A variable refractive index can be achieved by lengthening one of the lattice constants a_y compared to the lattice constant a_x in the orthogonal direction. Phase speeds $\bar{c}_{xx}$ and $\bar{c}_{yy}$ in the primary Cartesian directions are shown in Fig. 1(b) as a function of the anisotropy ratio a_y/a_x for a fixed aluminum tube outer radius $R = 0.4a_x$. The double index on the phase speeds delineates components in an anisotropic tensor. Phase speeds $\bar{c}$ with an overbar are normalized to the water background, which is assumed to have density $\rho_b = 1000\ \mathrm{kg/m^3}$ and sound speed $c_b = 1480\ \mathrm{m/s}$. The phase speeds are derived from the longitudinal dispersion bands of the acoustic band structure calculated for each anisotropy ratio. The anisotropy in phase speed can also be derived by considering multiple scattering effects in the lattice [21].

Examples of the acoustic band structure are shown in Figs. 1(c) and 1(d). Blue and red lines, with slopes corresponding to the phase speeds in Fig. 1(b), demonstrate that the longitudinal bands have linear dispersion up to an upper cutoff frequency $\omega a_x/2\pi c_b \simeq 0.3$. The cutoff frequency is constrained by the wrapping of the longitudinal band at the Brillouin zone boundary in the ΓY direction for the highest anisotropy ratio considered. The longitudinal band in the ΓM direction in Fig. 1(c) has a slowness that deviates slightly from circularity due to the underlying cubic symmetry. In addition to the longitudinal bands, narrow resonance bands arising from the core-shell architecture of the unit cell are predicted at various frequencies [5]. While we do not observe evidence of coupling to these bands in our measurements, the resonant bands should not, in general, be overlooked depending on the lattice geometry.

Our lens design consists of a constant lattice spacing in the x direction, which produces a flat lens facet, while a prescribed lattice anisotropy in the y direction produces the convex GRIN profile [see Fig. 2(b)]. The primary impact of increasing the anisotropy ratio is to decrease the effective sound speed irrespective of the propagation direction. As is evident in Fig. 1(b), the difference between $\bar{c}_{xx}$ and $\bar{c}_{yy}$ is small even at $a_y/a_x = 2$, resulting in approximately isotropic acoustic transport over the entire Brillouin zone. Therefore, an approximate, isotropic sound speed $\bar{c}_{\mathrm{avg}} = (\bar{c}_{xx} + \bar{c}_{yy})/2$ is used to initially guide the design of the GRIN geometry. A number of GRIN profiles that result in convex lensing are commonly used in the literature; our design combines two common refraction profiles in order to minimize lens aberration in the asymptotic (ray) transport limit:

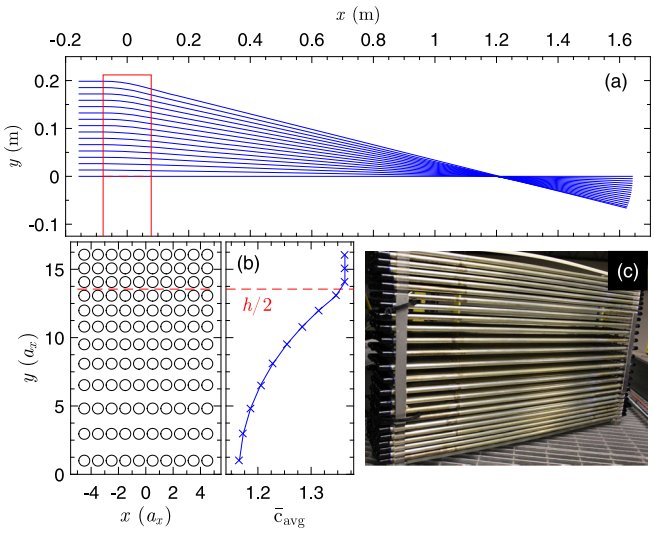

FIG. 2. (a) Ray paths through the lens (blue lines), which originate from a plane wave at normal incidence, are calculated using an eikonal approximation in the xy plane; the red box indicates the location of the lens. Only rays incident on the upper half-plane of the lens are shown. (b) Schematic showing the locations of the lattice sites in the upper half-plane of the lens; the resulting sound-speed profile is plotted to the right. The lattice sites are symmetric about $y = 0$. (c) Photograph of the assembled lens composed of 1-m-long, hollow aluminum cylinders arranged in the desired lattice pattern.

$$\bar{n}^2(y) = \frac{1}{[\bar{c}_{\mathrm{avg}}(y)]^2} = \left(\beta\frac{\bar{c}_0^2}{1-(\alpha_1 y)^2} + (1-\beta)\bar{c}_0^2(\cosh\alpha_2 y)^2\right)^{-1}, \quad (1)$$

$$\alpha_1 = (2/h)\sqrt{1-(\bar{c}_0/\bar{c}_h)^2}, \quad (2)$$

$$\alpha_2 = (2/h)\mathrm{arccosh}(\bar{c}_h/\bar{c}_0), \quad (3)$$

where h is the lens height in the gradient direction, $\bar{c}_0 = \bar{c}_{\mathrm{avg}}(0)$ and $\bar{c}_h = \bar{c}_{\mathrm{avg}}(h/2)$ are the extremal sound speeds obtained from the chosen range of the anisotropy ratio a_y/a_x, and β is a parameter that mixes the two GRIN profiles. The two GRIN profiles produce complementary aberrations: One causes ray trajectories that originate at the edge of the aperture to converge farther out along the focal plane, while the other causes rays from the aperture edge to converge closer in toward the lens. Mixing of the two GRIN profiles facilitates a condition where the rays can converge at a single point on the focal plane.

Lens aberration is commonly considered in the asymptotic limit of wave transport, where the aperture size is large and the index gradient is slowly varying compared to the acoustic wavelength. Although the lower portion of our operational bandwidth is close to the aperture diffraction limit, we utilize a ray-tracing routine in our design process for two specific purposes. First, we provide a recipe that details how our anisotropic lattice design can account for aberration assuming a targeted operational bandwidth that is closer to the aperture asymptotic limit. Second, we use ray trajectories, in parallel with the Huygens-Fresnel principle, to approximate the spatial distribution of the amplitude and phase of the acoustic signal over the surface of the lens facet. We demonstrate below that integration of this amplitude and phase information can accurately predict the impact of our finite aperture size on the focal patterns produced by the lens.

An iterative ray-tracing routine based on the eikonal approximation [22] is used to determine the optimal value of β that minimizes the lens aberration. The isotropic refraction gradient in Eq. (1) prescribes $\bar{c}_{\mathrm{avg}}(y)$ and hence the lattice geometry a_y/a_x for a given value of β; however, to optimize β, an eikonal approximation that accounts for the anisotropic sound speeds in the lattice is employed to more accurately predict the ray trajectories on the focal plane and hence the degree of aberration. The differential equation governing the eikonal function $\xi(\mathbf{x})$ in the presence of anisotropy can be derived for acoustic metafluids in a similar manner to the electromagnetic case [22]:

$$\bar{c}_{xx}^2\xi_x^2 + \bar{c}_{yy}^2\xi_y^2 - 2\bar{c}_{xy}^2\xi_x\xi_y = 1, \quad (4)$$

where $\xi_{[x,y]} = d\xi/d[x,y]$. The off-diagonal sound speed $\bar{c}_{xy}$ can be calculated from the band structure or by considering multiple scattering effects [21]. The off-diagonal term is found to be negligible compared to the on-diagonal terms for each anisotropy ratio in our lattice.

Figure 2(a) shows the ray paths derived using Eq. (4) for a GRIN lens insonified by a plane wave after optimizing the parameter β. The lens has thickness $10a_x$, height $h = 27.1a_x$, and lattice spacing $a_x = 15.6$ mm; these parameters are also used to manufacture the physical lens. The choice of $\beta = 0.65$ produces a focal point at $x_f \simeq 1.2$ m from the center of the lens with minimal aberration of the ray trajectories. The β optimization iterates within the interval $\beta = [0, 1]$ to identify the value that minimizes aberration. The optimization starts with the average sound speed profile $\bar{c}_{\mathrm{avg}}(y)$ as input and converts to the anisotropic phase speeds from Fig. 1(b). Anisotropic ray tracing is then used to predict the convergence of the ray trajectories on the focal plane. Note that, because the refraction gradient is produced by lengthening the lattice constant, the optimal GRIN profile described by Eqs. (1)–(3) must also be self-consistent with a discretization into lattice sites $a_y(y)$ that map back onto the analytic profile. This constrains the lens height h to certain values that produce a GRIN profile with minimal aberration while simultaneously conforming to a physically realizable lattice spacing.

III. EXPERIMENT

A schematic of the upper half of the β-optimized lens design is shown in Fig. 2(b). The full lens is symmetric

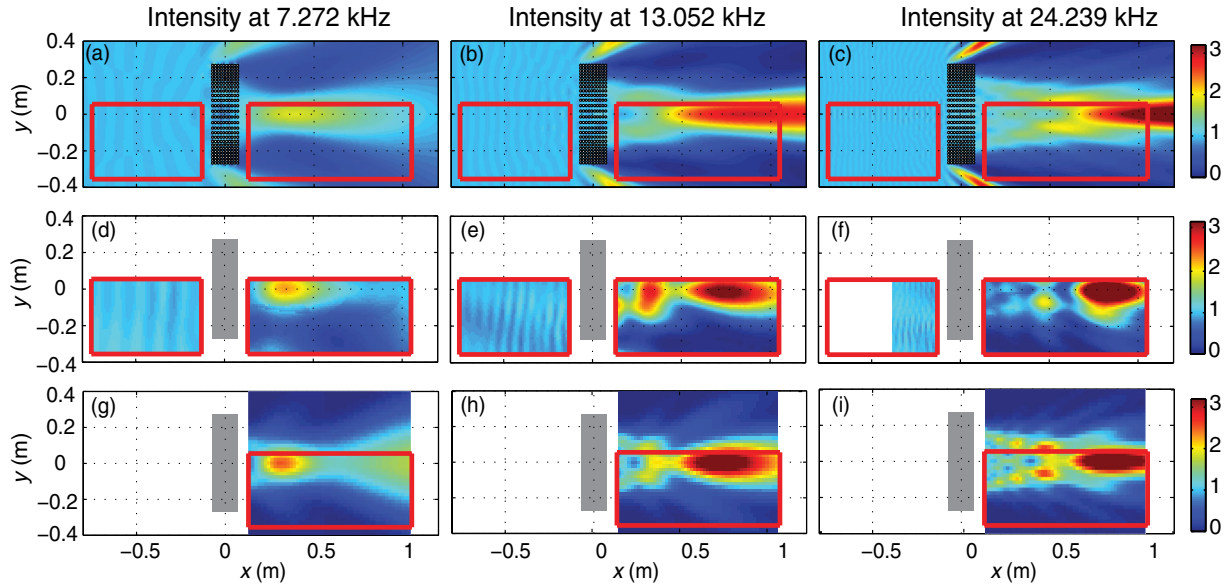

FIG. 3. Sound-pressure intensity in the vicinity of the lens at $\omega a_x/2\pi c_b = 0.077$ (7.27 kHz), 0.138 (13.05 kHz), and 0.256 (24.24 kHz) for a source location on the x axis. (a)–(c) Pressure intensity calculated using 2D MST. (d)–(f) Measured pressure intensity. (g)–(i) Pressure intensity calculated using a 3D Rayleigh-Sommerfeld approximation. Gray boxes show the position of the lens. Red outlines indicate the experimentally mapped areas. The reduced observational range of the reflected signal at 24.24 kHz is due to a limited overlap between the incident and reflected signals in the time domain at high frequency.

about the y axis. A photograph of the assembled lens is shown in Fig. 2(c). The lens is constructed of identical 1-m-long hollow aluminum cylinders with air inside. Each cylindrical tube has a diameter of 12.5 mm and a nominal wall thickness of 0.625 mm. Rubber end caps are adhered to both ends of each cylinder to prevent water infiltration. Additionally, approximately 2.5 cm of foam is inserted into the tube ends to damp the excitation of axial modes. The tubes are mounted on Plexiglas end plates into which holes with the designed lattice pattern are drilled. Two additional rows of cylinders with spacing $a_y = a_x$ are placed at the top and bottom of the lens to help mitigate the sharp transition where the edge of the lens ($\bar{c}_{\text{avg}} = 1.36$) meets the open water ($\bar{c}_{\text{avg}} = 1$).

The lens is submerged at the center of a $6 \times 6 \times 4$ m^3 water tank. Acoustic waves are produced by a 0.1-m-diameter spherical source located in the plane that bisects the lens midpoint in the axial direction (z axis). In order to demonstrate the lens directionality, two in-plane source locations are considered at $(x, y) = (-1.6, 0)$ m and $(x, y) = (-1.6, 0.43)$ m corresponding to incident angles of 0° and 15°, respectively, from the lens central axis (x axis). Wave propagation is measured using hydrophones at a sampling rate of 0.8 MHz. Hydrophones are mounted on a three-axis translation positioning system to record measurements of the sound-pressure levels $P(x, y)$ and $P_0(x, y)$ in the presence and absence of the lens, respectively. Measurements are taken at 10-mm increments. The sound-pressure level is measured at individual frequencies by averaging over a 10-cycle pulse in the transmission region (as indicated in Figs. 3 and 4) and a 20-cycle pulse in the reflection region. The longer pulse cycle used in the reflection region ensures overlap between the incident and reflected waves so that the measured total field can be properly compared with simulations. The length of the incident pulses are short enough to isolate reflections from the tank walls.

Measurements are performed in the xy plane perpendicular to the cylindrical axis of the lens over a broad range of frequencies $\omega a_x/2\pi c_b < 0.3$. Examples of the measured and numerically modeled pressure intensity $(|P|/|P_0|)^2$ in the vicinity of the lens are shown in Figs. 3 and 4 for frequencies $\omega a_x/2\pi c_b = 0.077$, 0.138, and 0.256. In both the measured and predicted results, the pressure intensity is normalized (at each position) to that of the source intensity in the absence of the lens. Given the symmetry of the lens about the y axis, measurements are obtained over the bottom half of the scattering plane with a small overlap into the upper half-plane to detail the on-axis forward-scattering pattern. The regions scanned in the measurement are also outlined in the upper panels in Figs. 3 and 4 for ease of comparison with the numerical predictions. Note that, although the measurements at $\omega a_x/2\pi c_b = 0.077$ and 0.256 lie within two of the resonance bands identified in Fig. 1, no obvious additional resonant features are observed in the intensity maps that can be attributed to these resonance bands.

We do not expect to observe attenuation due to viscous or thermal loss. For our measurement temperature of 293 K and the lowest operational frequency of 5 kHz, the viscous and thermal boundary layers in water are calculated to be 8 and 3 μm, respectively. These boundary layers are less than

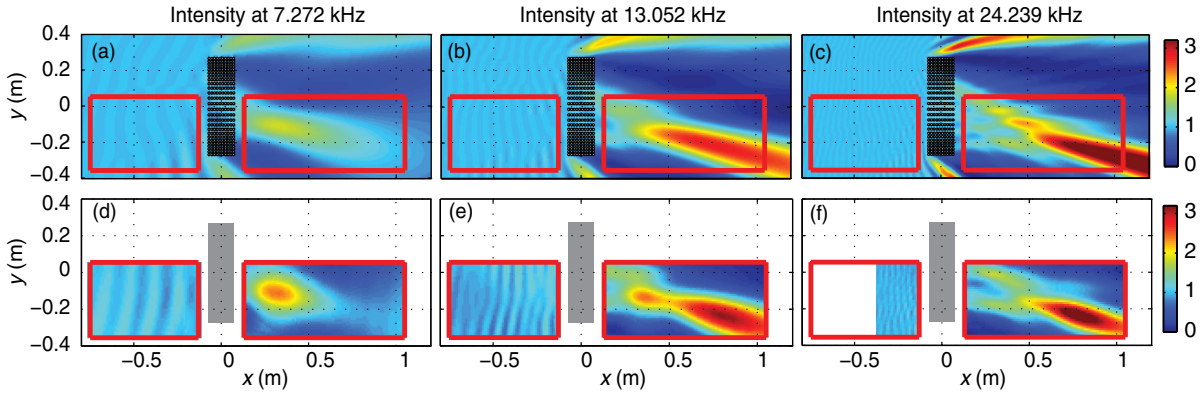

FIG. 4. Sound-pressure intensity in the vicinity of the lens at $\omega a_x/2\pi c_b = 0.077$ (7.27 kHz), 0.138 (13.05 kHz), and 0.256 (24.24 kHz) for a source positioned at a 15° angle with respect to the x axis. (a)–(c) Pressure intensity calculated using 2D MST. (d)–(f) Measured pressure intensity. Gray boxes show the position of the lens. Red outlines indicate the experimentally mapped areas.

0.3% of the smallest cylinder separation in our lattice, a value that is much lower than the approximately 5% threshold that was recently demonstrated to impact acoustic performance in small channels [23]. The impact of viscosity and heating is also derived for sonic crystal lattices composed of rigid [24] and elastic [25] scatterers, and the application of this theory to our lattice geometry under a rigid approximation results in a negligible dissipation factor of one part in a thousand.

IV. SIMULATIONS

The upper panels [(a)–(c)] in Figs. 3 and 4 show a prediction of the transmitted and reflected pressure intensity calculated using the two-dimensional multiple scattering theory (2D MST) [4,21]. The MST accounts for elastic scattering in the cylindrical tubes and assumes insonification by a cylindrical monopole source located at positions that match the experiment. Note that the MST predicts the acoustic pressure solely based on scattering from the lattice of tubes; it does not rely on approximations or ray tracing. The experimentally measured acoustic intensities in panels (d)–(f) show good qualitative agreement with the MST-predicted results. The reflected signal $R = 20\log_{10}[(P - P_0)/P_0)]$ is estimated relative to the incident amplitude P_0 using the sound-pressure level P measured in front of the incident face of the lens (regions to the left of the lens in Figs. 3 and 4). The measured reflection is at or below 13% of the incident amplitude ($R \leq -18$ dB) over the range of operational frequencies, which demonstrates significant transparency and is commensurate with recent Fresnel lens designs in air [26,27]. The measured reflection includes additional constructive interference compared to the MST due to diffraction from the finite aperture size in the axial direction.

In the forward direction, a focusing peak is observed that strengthens in intensity and moves out away from the lens with increasing frequency. The frequency dependence of the focusing peak is expected. At very low frequencies, the aperture is diffraction limited; as is the case for optical lenses [28], there is a focal shift toward the lens aperture as the Fresnel number $N = h^2/4\lambda x_f$ tends to zero. As the frequency increases, the transmission approaches the asymptotic limit of ray acoustics where a focusing peak would be located beyond the focal point predicted by the ray tracing in Fig. 2(a). At the lowest example frequency, $\omega a_x/2\pi c_b = 0.077$ [panels (a) and (d)], the lens is close to the diffraction limit with height-to-wavelength ratio $h/\lambda < 2$. As the frequency is further reduced, the focusing peak intensity becomes significantly suppressed. Therefore, an operational bandwidth can be identified ranging between $\omega a_x/2\pi c_b \approx 0.05$ and 0.30, where the lower cutoff is constrained by the diffraction limit and the upper cutoff by the homogenization limit of the lattice.

It is apparent in Figs. 3 and 4 that the 2D MST does not accurately predict the precise location of the intensity maxima nor the small-scale, near-field interference features in the forward direction. The discrepancy is due to the assumption of infinite cylinders in the 2D theory compared to the finite size of the lens aperture in the experiment. The diffractive corrections arising from the finite size in the axial direction can be predicted using a three-dimensional (3D) Rayleigh-Sommerfeld integral assuming knowledge of the acoustic amplitude and phase on the lens aperture. The pressure at a position (x, y, z) in front of an acoustic aperture located at $x = 0$ can be calculated by integrating over the aperture surface [29]:

$$P(x,y,z) = \frac{x}{i\lambda}\iint_A \tilde{P}(y',z')\frac{e^{ikr}}{r^2}dy'dz', \tag{5}$$

$$\tilde{P}(y',z') = \psi(y',z')e^{i\phi(y',z')}, \tag{6}$$

$$r^2 = x^2 + (y-y')^2 + (z-z')^2, \tag{7}$$

where $\psi(y',z')$ and $\phi(y',z')$ are the real-valued acoustic amplitude and phase of the complex pressure $\tilde{P}(y',z')$ on

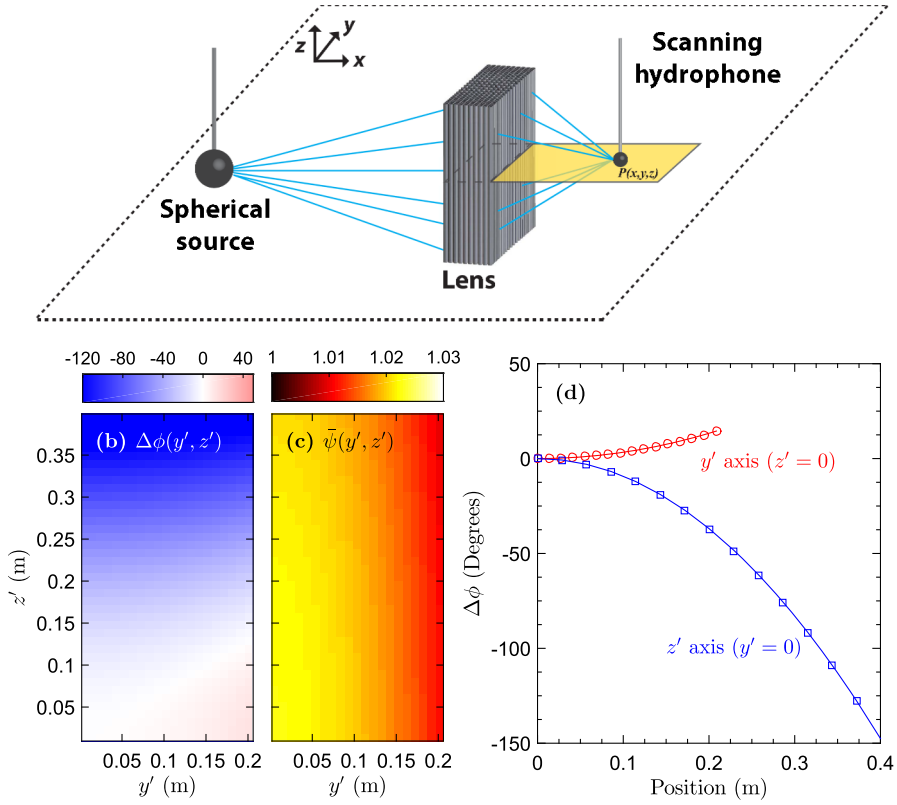

FIG. 5. (a) Schematic showing the experimental setup; blue lines indicate ray paths emerging from the spherical source and Rayleigh-Sommerfeld integration vectors from the forward facet of the lens to hydrophone locations in the measurement plane. (b) Change in phase $\Delta\phi(y',z')$ (degrees) over the forward facet (due to symmetry, only the first quadrant is shown). Blue regions represent a phase delay; red regions represent a phase advance. (c) Normalized amplitude $\bar{\psi}(y',z')$ over the forward facet, where normalization is with respect to the amplitude of the spherical wave in the absence of the lens. (d) Red and blue lines show the phase change $\Delta\phi$ plotted as a function of position along the y' and z' axis, respectively. Data points are calculated by advancing the phase along ray paths based on an eikonal approximation; lines are quadratic fits to the data.

the aperture facet, respectively, and λ and k are the wavelength and wave number, respectively. Here the integration aperture is simplified by the flat facet of our lens design, with the integration carried out over a simple rectangular area at the *forward* face of the lens.

The pressure on the aperture facet $\tilde{P}(y',z')$ can be estimated using anisotropic ray tracing under the eikonal approximation of Eq. (4). Although the eikonal approximation assumes a slowly varying refractive index on the scale of the wavelength, our results indicate reasonable empirical agreement with the experiment even at the lower frequencies close to the diffraction limit. A schematic in Fig. 5(a) depicts the ray trajectories of wave fronts that emerge from the spherical source and become incident on the lens aperture; integration vectors to a position (x,y,z) on the measurement plane are also depicted. The phase function $\phi(y',z')$ on the forward facet is determined by advancing the phase of each ray along the path lengths defined by $\xi(\mathbf{x})$, where the path length is the sum of the trajectory from the source to the rear facet plus the trajectory taken within the lens to the forward facet. The calculation iterates over a discrete set of rays that enter the *rear* facet (i.e., the incident face) at equally spaced intervals. Note that the effective path length is altered by the spatially dependent local sound speed in the lens. A constant phase is assumed at the surface of the spherical source.

The phase difference $\Delta\phi = \phi(y',z') - \phi(0,0)$ on the aperture surface is shown in Fig. 5(b), where positive or negative values represent a phase advance or delay, respectively, relative to the phase $\phi(y'=0,z'=0)$ on the lens central axis. The phase is calculated using the experimental source position on the lens central axis. Given the symmetry of the lens, only one quadrant is shown. Curve fits in Fig. 5(d) indicate that $\Delta\phi$ is approximately quadratic in both the y and z directions. The amplitude function $\psi(y',z')$ is inversely related to the square root of the local areal density of the rays. This is approximated by calculating the average nearest-neighbor separation of rays intersecting the forward facet; a relative amplitude $\bar{\psi}(y',z') = \psi(y',z')/\psi(0,0)$ can then be estimated from the inverse of this nearest-neighbor separation. Figure 5(c) shows the variation in $\bar{\psi}(y',z')$ after normalizing to the predicted amplitude in the absence of the lens. It is clear that the lens refraction has a minimal impact on the amplitude (<3%) and that the diffractive correction is primarily influenced by the change in phase over the aperture.

Following a similar procedure as used by Gao *et al.* [28], Eq. (5) is evaluated numerically within the 2D plane of the measurement using quadratic approximations to $\phi(y',z')$ and $\psi(y',z')$. Intensity maps produced by the Rayleigh-Sommerfeld integration are shown in Figs. 3(g)–3(i) and demonstrate significantly improved quantitative agreement with the experiment. As is the case for the measurement and MST modeling, the Rayleigh-Sommerfeld-based pressure intensities are normalized to the pressure intensity of the spherical source in the absence of the lens. The 3D

Rayleigh-Sommerfeld integration more accurately predicts both the location of the focal positions and their magnitude. The measured magnification in sound-pressure level ranges between 4.5 and 7.3 dB over the operational bandwidth. The 2D MST predicts magnifications that are as much as 40% lower than the measured values, whereas the magnifications predicted by the Rayleigh-Sommerfeld integration agree to within 10%. We emphasize that the 2D lattice focuses only along one axis (y axis), resulting in lower magnifications than would be produced by axisymmetric 3D designs [26,27]. The magnification can be increased by extending our 2D design to three dimensions using tubes bent into a toroid configuration [12,15].

V. CONCLUSIONS AND OUTLOOK

We now place our results in context with other recent metamaterial design concepts. Traditional underwater and ultrasound applications have achieved an impedance match by utilizing rubbers that have sound speeds less than water. While rubbers are used as components in transparent metafluid lattices [1], there have been other recent advances in acoustic impedance-matched designs. For example, negative-index complementary metamaterials are proposed to significantly enhance the transparency through aberrating materials [30]. Superfocusing from a flat lens geometry was recently explored in elastic plates where pulsed excitation is demonstrated to significantly improve the focal resolution below the diffraction limit [31,32]. Given that this technique relies on the interference of resonant lattice modes in the time domain, it should be readily applicable to flat-faceted acoustic lenses similar to our design.

A class of metafluids based on the concept of space coiling have also featured prominently in the literature [33–36]. Space-coiled Fresnel lens designs are reported that show significant focusing while utilizing a thin aperture compared to the wavelength [26,27]. Although the strength of the space-coiling design is the ability to significantly modify a phase within a confined space, there is a drawback that it can only delay the phase over a lengthened path; similar to rubbers in water, the effective sound speed of these devices is less than the background fluid. The space-coiling design has not yet been demonstrated in water, where common solids such as steel that might be used to confine the coils cannot be assumed to be perfectly rigid due to their significantly smaller density contrast with water—thus introducing the challenge of elastic coupling [37] that must be incorporated into any design strategy. Although the kinematic viscosity of water is less than that of air [23], recent measurements of air-borne space-coiled metamaterials [36] demonstrate significant attenuation, and we caution that viscous effects should not be neglected in aqueous designs.

Our design extends the reach of aqueous transparent metafluids to include the option of *phase advance* and decreased effective path length. While not necessarily required for traditional lensing, there are metamaterial applications that require higher sound speeds compared to the propagation medium [17–20,38], the most prominent of which is scattering reduction. The requirement of higher relative sound speeds features prominently in scattering-reduction designs based on both coordinate transformation [39–41] and scattering cancellation [42,43]. The realization of a high-sound-speed, transparent GRIN lens represents an important proof of concept: It demonstrates that phase-advance metafluids can be constructed with significant tunability in both sound speed and impedance, including the option of matched impedance. Given that the concept of core-shell lattice components has now been extended to also include core modification [5], a wide range of GRIN and anisotropic designs should be achievable in water based on metafluid lattices.

This work is supported by the Office of Naval Research.

[1] Christina J. Naify, Theodore P. Martin, Christopher N. Layman, Michael Nicholas, Abel L. Thangawng, David C. Calvo, and Gregory J. Orris, Underwater acoustic omnidirectional absorber, Appl. Phys. Lett. **104**, 073505 (2014).

[2] Rui-Qi Li, Xue-Feng Zhu, Bin Liang, Yong Li, Xin-Ye Zou, and Jian-Chun Cheng, A broadband acoustic omnidirectional absorber comprising positive-index materials, Appl. Phys. Lett. **99**, 193507 (2011).

[3] Alfonso Climente, Daniel Torrent, and José Sánchez-Dehesa, Omnidirectional broadband acoustic absorber based on metamaterials, Appl. Phys. Lett. **100**, 144103 (2012).

[4] Theodore P. Martin, Christopher N. Layman, Kimberly M. Moore, and Gregory J. Orris, Elastic shells with high-contrast material properties as acoustic metamaterial components, Phys. Rev. B **85**, 161103 (2012).

[5] Alexey S. Titovich and Andrew N. Norris, Tunable cylindrical shell as an element in acoustic metamaterial, J. Acoust. Soc. Am. **136**, 1601 (2014).

[6] Baile Zhang, Tucker Chan, and Bae-Ian Wu, Lateral Shift Makes a Ground-Plane Cloak Detectable, Phys. Rev. Lett. **104**, 233903 (2010).

[7] Ming Yin, Xiao Yong Tian, Hao Xue Han, and Di Chen Li, Free-space carpet-cloak based on gradient index photonic crystals in metamaterial regime, Appl. Phys. Lett. **100**, 124101 (2012).

[8] Daniel Torrent and José Sánchez-Dehesa, Acoustic metamaterials for new two-dimensional sonic devices, New J. Phys. **9**, 323 (2007).

[9] Alfonso Climente, Daniel Torrent, and José Sánchez-Dehesa, Sound focusing by gradient index sonic lenses, Appl. Phys. Lett. **97**, 104103 (2010).

[10] Theodore P. Martin, Michael Nicholas, Gregory J. Orris, Liang-Wu Cai, Daniel Torrent, and José Sánchez-Dehesa, Sonic gradient index lens for aqueous applications, Appl. Phys. Lett. **97**, 113503 (2010).

[11] Shasha Peng, Zhaojian He, Han Jia, Anqi Zhang, Chunyin Qiu, Manzhu Ke, and Zhengyou Liu, Acoustic far-field focusing effect for two-dimensional graded negative

refractive-index sonic crystals, Appl. Phys. Lett. **96**, 263502 (2010).
[12] Lorenzo Sanchis, Andrés Yánez, Pedro L. Galindo, Joaquín Pizarro, and Juan Martínez Pastor, Three-dimensional acoustic lenses with axial symmetry, Appl. Phys. Lett. **97**, 054103 (2010).
[13] Lucian Zigoneanu, Bogdan-Ioan Popa, and Steven A. Cummer, Design and measurements of a broadband two-dimensional acoustic lens, Phys. Rev. B **84**, 024305 (2011).
[14] Sz-Chin Steven Lin, Bernhard R. Tittmann, and Tony Jun Huang, Design of acoustic beam aperture modifier using gradient-index phononic crystals, J. Appl. Phys. **111**, 123510 (2012).
[15] T. M. Chang, G. Dupont, S. Enoch, and S. Guenneau, Enhanced control of light and sound trajectories with three-dimensional gradient index lenses, New J. Phys. **14**, 035011 (2012).
[16] A.-C. Hladky-Hennion, J. O. Vasseur, G. Haw, C. Croënne, L. Haumesser, and A. N. Norris, Negative refraction of acoustic waves using a foam-like metallic structure, Appl. Phys. Lett. **102**, 144103 (2013).
[17] Chunyu Ren, Zhihai Xiang, and Zhangzhi Cen, Design of acoustic devices with isotropic material via conformal transformation, Appl. Phys. Lett. **97**, 044101 (2010).
[18] Christopher N. Layman, Theodore P. Martin, Kimberly M. Moore, David C. Calvo, and Gregory J. Orris, Designing acoustic transformation devices using fluid homogenization of an elastic substructure, Appl. Phys. Lett. **99**, 163503 (2011).
[19] Martin Maldovan, Sound and heat revolutions in phononics, Nature (London) **503**, 209 (2013).
[20] Muamer Kadic, Tiemo Bückmann, Robert Schittny, and Martin Wegener, Metamaterials beyond electromagnetism, Rep. Prog. Phys. **76**, 126501 (2013).
[21] D. Torrent and J. Sánchez-Dehesa, Anisotropic mass density by two-dimensional acoustic metamaterials, New J. Phys. **10**, 023004 (2008).
[22] Claudio G. Parazzoli, Benjamin E. C. Koltenbah, Robert B. Greegor, Tai A. Lam, and Minas H. Tanielian, Eikonal equation for a general anisotropic or chiral medium: Application to a negative-graded index-of-refraction lens with an anisotropic material, J. Opt. Soc. Am. B **23**, 439 (2006).
[23] G. P. Ward, R. K. Lovelock, A. R. J. Murray, A. P. Hibbins, J. R. Sambles, and J. D. Smith, Boundary-Layer Effects on Acoustic Transmission through Narrow Slit Cavities, Phys. Rev. Lett. **115**, 044302 (2015).
[24] Matthew D. Guild, Victor M. García-Chocano, Weiwei Kan, and José Sánchez-Dehesa, Acoustic metamaterial absorbers based on multilayered sonic crystals, J. Appl. Phys. **117**, 114902 (2015).
[25] Edgar Reyes-Ayona, Daniel Torrent, and José Sánchez-Dehesa, Homogenization theory for periodic distributions of elastic cylinders embedded in a viscous fluid, J. Acoust. Soc. Am. **132**, 2896 (2012).
[26] Miguel Molerón, Marc Serra-Garcia, and Chiara Daraio, Acoustic fresnel lenses with extraordinary transmission, Appl. Phys. Lett. **105**, 114109 (2014).
[27] Yong Li, Gaokun Yu, Bin Liang, Xinye Zou, Guangyun Li, Su Cheng, and Jianchun Cheng, Three-dimensional ultrathin planar lenses by acoustic metamaterials, Sci. Rep. **4**, 6830 (2014).
[28] Yang Gao, Jianlong Liu, Xueru Zhang, Yuxiao Wang, Yinglin Song, Shutian Liu, and Yan Zhang, Analysis of focal-shift effect in planar metallic nanoslit lenses, Opt. Express **20**, 1320 (2012).
[29] M. Born and E. Wolf, *Electromagnetic Theory of Propagation, Interference and Diffraction of Light*, seventh ed. (Cambridge University Press, Cambridge, England, 1999).
[30] Chen Shen, Jun Xu, Nicholas X. Fang, and Yun Jing, Anisotropic Complementary Acoustic Metamaterial for Canceling out Aberrating Layers, Phys. Rev. X **4**, 041033 (2014).
[31] M. Dubois, M. Farhat, E. Bossy, S. Enoch, S. Guenneau, and P. Sebbah, Flat lens for pulse focusing of elastic waves in thin plates, Appl. Phys. Lett. **103**, 071915 (2013).
[32] M. Dubois, E. Bossy, S. Enoch, S. Guenneau, G. Lerosey, and P. Sebbah, Time-Driven Superoscillations with Negative Refraction, Phys. Rev. Lett. **114**, 013902 (2015).
[33] W. E. Kock and F. K. Harvey, Refracting sound waves, J. Acoust. Soc. Am. **21**, 471 (1949).
[34] Zixian Liang and Jensen Li, Extreme Acoustic Metamaterial by Coiling up Space, Phys. Rev. Lett. **108**, 114301 (2012).
[35] Yangbo Xie, Adam Konneker, Bogdan-Ioan Popa, and Steven A. Cummer, Tapered labyrinthine acoustic metamaterials for broadband impedance matching, Appl. Phys. Lett. **103**, 201906 (2013).
[36] Tobias Frenzel, Jan David Brehm, Tiemo Bckmann, Robert Schittny, Muamer Kadic, and Martin Wegener, Three-dimensional labyrinthine acoustic metamaterials, Appl. Phys. Lett. **103**, 061907 (2013).
[37] Andrey Bozhko, Victor M. García-Chocano, José Sánchez-Dehesa, and Arkadii Krokhin, Redirection of sound in straight fluid channel with elastic boundaries, Phys. Rev. B **91**, 094303 (2015).
[38] C. García-Meca, S. Carloni, C. Barceló, G. Jannes, J. Sánchez-Dehesa, and A. Martínez, Transformational acoustic metamaterials based on pressure gradients, Phys. Rev. B **90**, 024310 (2014).
[39] Steven A Cummer and David Schurig, One path to acoustic cloaking, New J. Phys. **9**, 45 (2007).
[40] Huanyang Chen and C. T. Chan, Acoustic cloaking in three dimensions using acoustic metamaterials, Appl. Phys. Lett. **91**, 183518 (2007).
[41] Steven A. Cummer, Bogdan-Ioan Popa, David Schurig, David R. Smith, John Pendry, Marco Rahm, and Anthony Starr, Scattering Theory Derivation of a 3D Acoustic Cloaking Shell, Phys. Rev. Lett. **100**, 024301 (2008).
[42] Matthew D. Guild, Michael R. Haberman, and Andrea Alù, Plasmonic-type acoustic cloak made of a bilaminate shell, Phys. Rev. B **86**, 104302 (2012).
[43] Theodore P. Martin and Gregory J. Orris, Hybrid inertial method for broadband scattering reduction, Appl. Phys. Lett. **100**, 033506 (2012).